Computation of the Tip Vortex Off a Low-Aspect-Ratio Wing

N. N. Mansour*
Stanford University, Stanford, California

The viscous transonic flow around a low-aspect-ratio wing has been computed using an implicit, three-dimensional, "thin-layer" Navier-Stokes solver. The grid around the geometry of interest is obtained numerically as a solution to a Dirichlet problem for the cube. The geometry chosen for this study is a low-aspect-ratio wing with large sweep, twist, taper, and camber. The topology chosen to wrap the mesh around the wing with good tip resolution is a C-O-type mesh. Using this grid, the flow around the wing was computed for a freestream Mach number of 0.82 at an angle of attack of 5 deg. At this Mach number, an oblique shock forms on the upper surface of the wing, and a tip vortex and three-dimensional flow separation off the wing surface are observed. Particle path lines indicate that the three-dimensional flow separation on the wing surface is a part of the root of the tip-vortex formation. The lifting of the tip vortex before the wing trailing edge is clearly observed by following the trajectory of particles released around the wing tip.

Introduction

IT is well known from classic wing theory[1] that the presence of a vortex wake is a necessary condition for all finite-span lifting wings. The most advanced full-potential numerical methods for the simulation of subsonic and transonic flows combine classic wing theory (vortex sheet trailing the wing at a fixed spatial location) with the full-potential calculation to compute realistic lift values for wings of fairly general shapes.[2] In reality, this vortex sheet will roll up into discrete vortices.[1] This rollup starts close to the wing tip where the flow is predominantly three dimensional and possesses a concentrated (rolled-up) vortex structure. The wake vortex generated by large transport aircraft is known for its potential hazard to smaller aircraft. This hazard is the major impediment to increasing traffic capacity at major air terminals and a large effort is being directed to minimize it.[3] In the case of low-aspect-ratio wings, the tip vortex contributes directly to lift and drag and, hence, is important in practical applications.

To contribute to our understanding of the formation of the tip vortex, a mathematical model is needed in which the appearance of the tip vortex is a result of the solution rather than an empirical input to the solution. At high Reynolds numbers, the simplest model seems to be the thin-layer approximation[4] to the Navier-Stokes equations, since the vortex formation is a viscous phenomenon generated in a thin layer close to the surface of the wing, whereas most of the flowfield is convection dominated. The model that incorporates the full viscous terms is preferable when a fine mesh is used in all three directions. However, experience with two-dimensional computations indicates that the difference between the results from a full Navier-Stokes calculation and a thin-layer calculation is negligible when a coarse grid is used in the streamwise direction. The objective of this paper is to study the formation of the tip vortex off a low-aspect-ratio wing. The thin-layer approximation is used as a first model for this purpose. Vortex formation and capturing at wing tips are reported by Rizzi and Eriksson[5] and Eriksson and Rizzi[6] who use the Euler equations as the mathematical model. It is not clear why a tip vortex is observed in inviscid (Euler) flow computations, and the understanding of this observation is still under investigation by Rizzi.[7]

Considerable progress has been made in developing the solution methods for the nonlinear equations of fluid motion. For a review of the achievements of the numerical methods in computing transonic flows, the reader is referred to Ref. 8. The methods range from the fully explicit to the factored fully implicit schemes. The application of these methods to three-dimensional flows has been restricted primarily to simple geometries. Both the computational efforts involved and the problem of grid generation over complicated geometries seem to hinder the application of the available computational methods to three dimensions.

The procedure followed in this work is to treat the mesh-generation problem and the solution to the governing equations as two separate operations. This appears to be the approach followed by most authors[6,9,10] to compute the three-dimensional flow over complicated geometries. The adaptive gridding approach[11] is still under development, and its application to three dimensions for complicated geometries is still not proved. The mesh-generation method chosen to generate the grid around the geometry of interest is an elliptic mesh generator. The geometry chosen for this study is a low-aspect-ratio ($A_r = 0.85$) wing with 45 deg sweep, 8.3 deg twist, and 0.3 taper. The mathematical model used to compute the flow around this wing is the thin-layer Navier-Stokes equations in generalized coordinates. The numerical method used to solve these equations is the factored implicit scheme[12,13] as applied to three-dimensional aerodynamics applications by Pulliam and Steger.[14] A data-management strategy is adopted to allow the use of fairly fine three-dimensional meshes (up to 200,000 grid nodes). The computed results (using 75,000 grid points) for the formation of the tip vortex over a low-aspect-ratio wing at a transonic Mach number ($M = 0.82$) are presented in the Results section.

Grid Generation

The grid around the geometry of interest is obtained numerically as a solution to a Dirichlet problem for the cube. The approach relies on the method of Mastin and Thompson,[15] with the source terms specified using a variation of the method of Thomas.[16] The source terms in this approach are specified so that the Poisson equations possess exponential solutions for locally constant parameters. This allows grid control inside the volume by the grid-point distribution assigned on the surface of the domain. The

Presented as Paper 84-0522 at the AIAA 22nd Aerospace Sciences Meeting, Reno, Nev., Jan. 9-12, 1984; received Feb. 24, 1984; revision received Sept. 17, 1984.

*Senior Research Associate; presently, Aerospace Engineer, NASA Ames Research Center, Moffett Field, Calif. Member AIAA.

distribution on the surface of the domain is controlled by the grid-point distribution along the boundary of the surface using the method of Thomas and Middlecoff.[17]

Generation Procedure

The first task is to distribute the grid points on the boundary of the six surfaces of the volume of interest. This is done using a composite transformation consisting of hyperbolic-tangent and hyperbolic-sine functions as follows[18]:

$$a(x-x_0)=\sinh(c\Gamma+d) \tag{1}$$

$$e\xi+f=\tanh^{-1}(g\Gamma+h) \tag{2}$$

where x is the physical coordinate $\in[x_1,x_2]$, ξ the transformed coordinate $\in[1,N]$, and Γ an intermediate coordinate $\in[1,N]$; N is the total number of grid points. To determine the seven constants a, c, d, e, f, g, and h, the following four conditions are imposed:

$$\xi=1,\ \Gamma=1 \text{ when } x=x_1, \text{ and } \xi=N,\ \Gamma=N \text{ when } x=x_2 \tag{3}$$

Three adjustable stretching parameters remain that are specified as follows:

$$t_1=g+h,\quad t_2=gN+h,\quad t_3=cN+d \tag{4}$$

Parameters t_1 and t_2 provide grid clustering around x_1 and x_2, and t_3 provides grid clustering around x_0.

Once the distribution of the grid points on the boundary of the surface has been determined, the two-dimensional elliptic grid-generation method of Thomas[16] is used to distribute the grid points on the surface.

In the above formulations, the boundary is assumed to be rectilinear and the surface is assumed to be planar. For general lines (or surfaces) the grid is generated on an appropriate rectilinear (or planar) projection, and the points on the line (or surface) are deduced from the points on the projection. A more general method that accounts for the effects of curvature would require specifying the tangents and radii of curvature, which, in general, may not be known analytically.

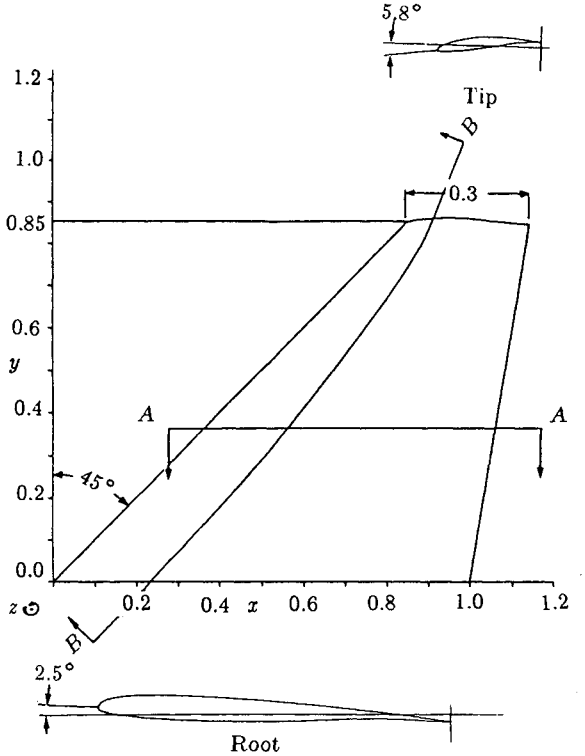

Fig. 1 Low-aspect-ratio wing geometry.

Once the grid is generated on the six surfaces of the volume, the mapping between the physical (x,y,z) and computational (ξ,η,ζ) space is determined by solving the following set of transformed Poisson equations:

$$\begin{aligned}
&\alpha_1(x_{\xi\xi}+\phi x_\xi)+\alpha_2(x_{\eta\eta}+\psi x_\eta)+\alpha_3(x_{\zeta\zeta}+\omega x_\zeta)\\
&\quad+2(\beta_1 x_{\xi\eta}+\beta_2 x_{\eta\zeta}+\beta_3 x_{\zeta\xi})=0\\
&\alpha_1(y_{\xi\xi}+\phi y_\xi)+\alpha_2(y_{\eta\eta}+\psi y_\eta)+\alpha_3(y_{\zeta\zeta}+\omega y_\zeta)\\
&\quad+2(\beta_1 y_{\xi\eta}+\beta_2 y_{\eta\zeta}+\beta_3 y_{\zeta\xi})=0\\
&\alpha_1(z_{\xi\xi}+\phi z_\xi)+\alpha_2(z_{\eta\eta}+\psi z_\eta)+\alpha_3(z_{\zeta\zeta}+\omega z_\zeta)\\
&\quad+2(\beta_1 z_{\xi\eta}+\beta_2 z_{\eta\zeta}+\beta_3 z_{\zeta\xi})=0
\end{aligned} \tag{5}$$

where

$$\begin{aligned}
\alpha_1&=\xi_x^2+\xi_y^2+\xi_z^2 & \beta_1&=\xi_x\eta_x+\xi_y\eta_y+\xi_z\eta_z\\
\alpha_2&=\eta_x^2+\eta_y^2+\eta_z^2 & \beta_2&=\eta_x\zeta_x+\eta_y\zeta_y+\eta_z\zeta_z\\
\alpha_3&=\zeta_x^2+\zeta_y^2+\zeta_z^2 & \beta_3&=\zeta_x\xi_x+\zeta_y\xi_y+\zeta_z\xi_z
\end{aligned} \tag{6}$$

The metric terms $\xi_x,\xi_y,\ldots$ are expressed in terms of $x_\xi,x_\eta,\ldots$ as follows:

$$\begin{aligned}
\xi_x&=J(y_\eta z_\zeta-y_\zeta z_\eta) & \eta_x&=J(z_\xi y_\zeta-z_\zeta y_\xi)\\
\xi_y&=J(z_\eta x_\zeta-z_\zeta x_\eta) & \eta_y&=J(x_\xi z_\zeta-x_\zeta z_\xi)\\
\xi_z&=J(x_\eta y_\zeta-x_\zeta y_\eta) & \eta_z&=J(y_\xi x_\zeta-y_\zeta x_\xi)
\end{aligned}$$

$$\begin{aligned}
\zeta_x&=J(y_\xi z_\eta-y_\eta z_\xi)\\
\zeta_y&=J(z_\xi x_\eta-z_\eta x_\xi)\\
\zeta_z&=J(x_\xi y_\eta-x_\eta y_\xi)
\end{aligned} \tag{7}$$

and

$$J^{-1}=x_\xi y_\eta z_\zeta+x_\zeta y_\xi z_\eta+x_\eta y_\zeta z_\xi-x_\xi y_\zeta z_\eta-x_\zeta y_\eta z_\xi-x_\eta y_\xi z_\zeta \tag{8}$$

Direct extension of the two-dimensional formulation to three dimensions yields the values of ϕ, ψ, and ω on the boundary as follows:

$$\begin{aligned}
&\phi=-(x_\xi x_{\xi\xi}+y_\xi y_{\xi\xi}+z_\xi z_{\xi\xi})/(x_\xi^2+y_\xi^2+z_\xi^2)\\
&\quad\text{on } \eta=1,N_\eta \text{ and } \zeta=1,N_\zeta\\
&\psi=-(x_\eta x_{\eta\eta}+y_\eta y_{\eta\eta}+z_\eta z_{\eta\eta})/(x_\eta^2+y_\eta^2+z_\eta^2)\\
&\quad\text{on } \xi=1,N_\xi \text{ and } \zeta=1,N_\zeta\\
&\omega=-(x_\zeta x_{\zeta\zeta}+y_\zeta y_{\zeta\zeta}+z_\zeta z_{\zeta\zeta})/(x_\zeta^2+y_\zeta^2+z_\zeta^2)\\
&\quad\text{on } \xi=1,N_\xi \text{ and } \eta=1,N_\eta
\end{aligned} \tag{9}$$

The continuous representation of the parameters is found in planes ξ, η, and $\zeta=$ const by solving the following equations analytically:

$$\phi_{\eta\eta\zeta\zeta}=0,\quad \psi_{\xi\xi\zeta\zeta}=0,\quad \omega_{\xi\xi\eta\eta}=0 \tag{10}$$

The solutions to Eqs. (10) are elementary extensions of the one-dimensional linear interpolation method to two dimensions.

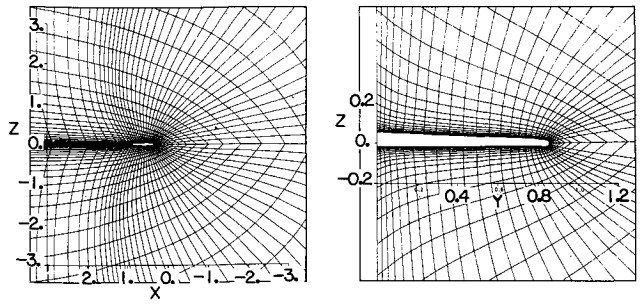

a) Section A-A. b) Section B-B.

Fig. 2 Grid distribution.

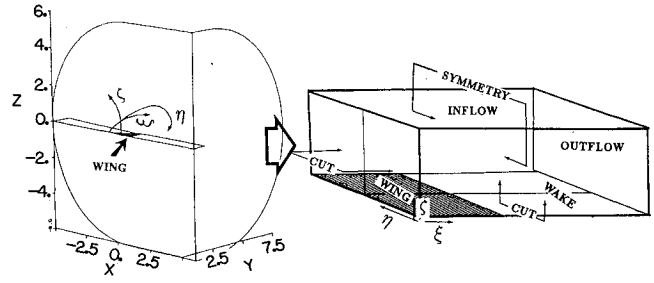

Fig. 3 Grid wrap.

Grid Type

The geometry chosen for this study is the low-aspect-ratio wing (wing C) investigated experimentally and numerically by Hinson and Burdges[19] and Keener.[20] The same geometry was also investigated numerically by Holst et al.[21] The characteristics of the wing are described in Fig. 1: 0.85 aspect ratio, 45 deg sweep, 8.3 deg twist, 0.3 taper. In these numerical studies, the full-potential equation was used to compute the flow around the wing. With the full-potential methods, the vortex sheets are fitted rather than captured, and, therefore, the wrap around the wing tip is not critical. If the flow around the wing tip is of interest, then a mesh that wraps around the tip is desirable. Different grid wraps can be used to resolve the flowfield around the wing that will achieve for a given total number of grid points concentration of grid points in different regions of the field. Rizzi and Eriksson[5] used the density of grid points around the wing as a criterion to judge the different grid wraps and concluded that O-O and C-O are the two "best" types. The C-O-type mesh shown in Fig. 2 was chosen in this study.

As pointed out by Rizzi and Eriksson, in order to map the wrap into a box-like region artificial singular lines need to be introduced. The location of these lines should be away from areas of interest since the flowfield in the neighborhood of these lines may be in doubt. The map into the computational box chosen for this study is shown in Fig. 3. The cuts were chosen to be on the leading and trailing edges, leaving the area around the tip free from these cuts. The wing and wake surface is mapped into the "bottom" surface of the parametric box (plane $\zeta=1$); the outer boundary (except the downstream surface) is mapped into the "top" surface (plane $\zeta=N_\zeta$); the upper plane of symmetry is mapped into the "front" surface of the box (plane $\eta=1$); the lower plane of symmetry is mapped into the "back" surface of the box (plane $\eta=N_\eta$); the cut at the leading edge is mapped into the "left" surface of the box (plane $\xi=1$); and the downstream surface of the outer boundary plane is mapped into the "right" surface of the box (plane $\xi=N_\xi$).

Governing Equations

At high Reynolds numbers, the flow around the wing can be considered to be mostly inviscid, except in a thin-layer region close to the body where the viscous effects become important. With this in mind, the thin-layer approximation is used to simplify the Navier-Stokes equations in generalized coordinates to yield[14]

$$\partial_\tau q+\partial_\xi E+\partial_\eta F+\partial_\zeta G=Re^{-1}\partial_\zeta S \tag{11}$$

where

$$q=J^{-1}\begin{bmatrix}\rho\\ \rho u\\ \rho v\\ \rho w\\ e\end{bmatrix},\qquad E=J^{-1}\begin{bmatrix}\rho U\\ \rho uU+\xi_x p\\ \rho vU+\xi_y p\\ \rho wU+\xi_z p\\ (e+p)U\end{bmatrix}$$

$$F=J^{-1}\begin{bmatrix}\rho V\\ \rho uV+\eta_x p\\ \rho vV+\eta_y p\\ \rho wV+\eta_z p\\ (e+p)V\end{bmatrix},\qquad G=J^{-1}\begin{bmatrix}\rho W\\ \rho uW+\zeta_x p\\ \rho vW+\zeta_y p\\ \rho wW+\zeta_z p\\ (e+p)W\end{bmatrix} \tag{12}$$

$$S=J^{-1}\begin{bmatrix}0\\ \mu_e(\zeta_x^2+\zeta_y^2+\zeta_z^2)u_\zeta+(\mu_e/3)(\zeta_x u_\zeta+\zeta_y v_\zeta+\zeta_z w_\zeta)\zeta_x\\ \mu_e(\zeta_x^2+\zeta_y^2+\zeta_z^2)v_\zeta+(\mu_e/3)(\zeta_x u_\zeta+\zeta_y v_\zeta+\zeta_z w_\zeta)\zeta_y\\ \mu_e(\zeta_x^2+\zeta_y^2+\zeta_z^2)w_\zeta+(\mu_e/3)(\zeta_x u_\zeta+\zeta_y v_\zeta+\zeta_z w_\zeta)\zeta_z\\ \{(\zeta_x^2+\zeta_y^2+\zeta_z^2)[0.5\mu_e(u^2+v^2+w^2)_\zeta\\ +\mu_e Pr^{-1}(\gamma-1)^{-1}T_\zeta]\\ +(\mu_e/3)(\zeta_x u+\zeta_y v+\zeta_z w)(\zeta_x u_\zeta+\zeta_y v_\zeta+\zeta_z w_\zeta)\}\end{bmatrix} \tag{13}$$

and

$$U=\xi_x u+\xi_y v+\xi_z w$$

$$V=\eta_x u+\eta_y v+\eta_z w$$

$$W=\zeta_x u+\zeta_y v+\zeta_z w \tag{14}$$

where U, V, and W are contravariant velocity components written without metric normalization. The above set of equations is nondimensionalized using a_∞ (the freestream sound speed) for velocity, the chord length c at the root of the wing for distances, and ρ_∞ the freestream density for density. One more equation of state is needed to close the above system, and the perfect gas law is used to relate the pressure, density,

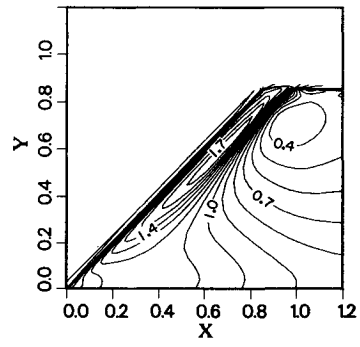

Fig. 4 Mach contours on a surface parallel to the wing surface. Contour intervals = 0.1.

and velocity as follows:

$$p=(\gamma-1)\,[e-0.5\rho(u^2+v^2+w^2)\,] \tag{15}$$

The effective viscosity in Eq. (13) is set equal to

$$\mu_e=1+\mu_t \tag{16}$$

where μ_t is a turbulent viscosity computed using the two-layer algebraic viscosity model of Baldwin and Lomax.[4]

Numerical Method

The approach followed in this work is the same as the one developed by Pulliam and Steger.[14] The numerical algorithm is the implicit noniterative approximate factorization scheme of Beam and Warming.[12] Fourth-order dissipation terms are added to the equations to control nonlinear instabilities, and implicit second difference terms operating on Δq are added to extend the linear stability bound of the fourth-order terms.

Linearization and Approximate Factorization

The equations of motion are differenced using a standard (nonstaggered) mesh, central differencing in space, and backward (fully implicit) differencing in time. The differenced equations are linearized in time, then factored using the Douglas and Gunn[22] technique to reduce the three-dimensional problem to three one-dimensional problems at a given time level. The differenced equations are written as follows:

$$D_\xi D_\eta D_\zeta \Delta q = H \tag{17}$$

where

$$\Delta q = q^{n+1}-q^n$$

$$D_\xi = I + h\delta_\xi \frac{\partial E^n}{\partial q^n} - \epsilon_I J^{-1} \nabla_\xi \Delta_\xi J$$

$$D_\eta = I + h\delta_\eta \frac{\partial F^n}{\partial q^n} - \epsilon_I J^{-1} \nabla_\eta \Delta_\eta J$$

$$D_\zeta = I + h\delta_\zeta \frac{\partial G^n}{\partial q^n} - hRe^{-1}\delta_\zeta \frac{\partial S^n}{\partial q^n} - \epsilon_I J^{-1} \nabla_\zeta \Delta_\zeta J$$

$$H = -\Delta t(\delta_\xi E^n + \delta_\eta F^n + \delta_\zeta G^n - Re^{-1}\delta_\zeta S^n)$$
$$-\epsilon_E J^{-1}[(\nabla_\xi\Delta_\xi)^2 + (\nabla_\eta\Delta_\eta)^2 + (\nabla_\zeta\Delta_\zeta)^2]Jq^n \tag{18}$$

The δ's are central-difference operators, ∇ and Δ are backward- and forward-difference operators, and $h=\Delta t$ is the time step. For a detailed description of the Jacobian matrices $\partial E^n/\partial q^n$, $\partial F^n/\partial q^n$, $\partial G^n/\partial q^n$, and $\partial S^n/\partial q^n$, the interested reader is referred to Ref. 14.

Data Management

Proper resolution of the flowfield around the wing requires a large number of grid points. Chapman[23] estimated the following requirements to resolve the three-dimensional boundary layer on a wing:

$$N_\xi = 4.5 n_\xi Re_c^{0.2}, \quad N_\eta = 4.5 A_r n_\eta Re_c^{0.2}, \quad N_\zeta = n_\zeta \tag{19}$$

where n_ξ, n_η, and n_ζ are the average number of grid points per length δ (the boundary-layer thickness) in the streamwise, spanwise, and normal directions, respectively; A_r the aspect ratio; and Re_c the Reynolds number based on the chord length. For $Re_c=1\times10^6$, $A_r=0.85$, $n_\xi=0.4$, $n_\eta=0.4$, and $n_\zeta=15$, we need $N_\xi=30$, $N_\eta=30$, and $N_\zeta=15$ to resolve the boundary layer on the upper surface. (Chapman recommends using $n_\xi=1$, $n_\eta=0.5$, and $n_\zeta=20$.) Adding 10 grid points in the ξ direction to capture the wake, doubling the grid points in the η direction to resolve the lower surface, and adding 15 grid points in the ζ direction for the outer inviscid field yields a required total number of grid ponts equal to 72,000. Nineteen words of memory are needed at each grid point to store the independent variables and the metrics; the required total number of words of memory is then 1.4×10^6. The Cray 1-S machine available at NASA Ames Research Center is nominally a 1×10^6 words-in-core-memory machine. The disk is then needed to store the flowfield data. To carry out the computation, part of the data is transferred into the core memory of the machine. The data-management algorithm devised is a five-plane algorithm.

The flowfield is stored on the solid-state disk (SSD) and the "in-core" working set is a slab of five planes. With this scheme, data are transferred to the core of the machine in ξ-η planes. When the data are needed in the ζ direction in more than five planes (for example, for matrix inversion), a sweep through the data is carried out. The sweep through the data occurs in the ζ direction only. For a matrix inversion in the ζ direction, two data sweeps are needed. The solution proceeds as follows: during the first data sweep, two matrices are inverted in each ξ-η plane. Also, forward elimination for the third matrix inversion is completed. During the second sweep, the inversion of the third matrix is completed and the solution is advanced. A mesh up to 200,000 grid points can be handled by this algorithm.

Boundary Conditions

The physical boundary conditions are the conditions at infinity and the no-slip conditions on the wing surface. However, additional boundary conditions are needed when the equations are discretized. In general, boundary conditions on the six surfaces of the computational box are required to close the system of differenced equations. The use of appropriate boundary conditions is dependent on the mesh wrap. The type of boundary conditions used with the C-O wrap in our case is shown in Fig. 3. At $\xi=1$, "cut" conditions are imposed. The cut boundary condition used in the present scheme is that the values at the cut are given as the average value of the two neighboring points in the computational domain. At $\xi=N_\xi$, exit boundary conditions are imposed where the values at the boundary are extrapolated from the interior of the domain along ξ lines. At $\eta=1$ and N_η, symmetry boundary conditions are imposed. At $\xi=1$, no-slip boundary conditions are imposed on the surface of the wing and cut conditions are imposed in the wake. At $\zeta=N_\zeta$, inflow conditions are imposed where the velocity, density, and Mach numbers are specified.

Results

Using the C-O-type mesh, the flow around the wing was computed for a freestream Mach number $M=0.82$ at an angle of attack $\alpha=5$ deg. The design conditions[19] for this wing were $M=0.85$ and $\alpha=5$ deg. Hence, the results presented in this section are for a Mach number slightly below the design Mach number, and the flow around the wing is expected to be smooth. (Smooth flow is loosely defined herein as a flow that does not exhibit a massive separation.) On average, 15 grid points were used to capture the boundary layer, the first plane parallel to the wing surface is at $y^+<7$. A five-order-of-magnitude drop in the residuals was achieved after 25 h of CPU time on the NASA Ames Cray 1-S machine. The computations were continued for several more hours to check that a steady-state solution was reached.

The Mach contours (Fig. 4) on a surface parallel to the wing surface show the presence of an oblique shock between $y\simeq0.4c$ and $0.75c$ at about 0.25 of the local chord length

from the leading edge. This shock is also detected by the C_p profiles of the experimental data. In the region of the shock, our mesh is relatively coarse, as can be seen in Fig. 5 where the open symbols represent the computed C_p results at the mesh locations. Comparison of the computed C_p profile with the experimental data shows that the suction peak is overpredicted. No Mach number or angle-of-attack corrections (for the presence of the walls in the experiment) were attempted to match the experimental data. Using the full-potential-equation formulation, Subramanian et al.[2] found that by correcting the Mach number and angle of attack they can match the experimental data at the different spanwise locations. In general, the shape of the C_p profiles predicted by the present computation is similar to the experimental profiles at the various spanwise locations, but the suction peak is overpredicted.

The flow pattern over the wing surface was visualized experimentally by Keener[20] using an oil-flow technique. It was found that, for low Mach numbers ($M<0.85$), the flow is smooth over the wing, but at high Mach numbers ($M>0.85$) a massive three-dimensional separation is observed on the upper surface of the wing. The oil-flow pattern for $M=0.82$ is shown in Fig. 6. The major feature of the flow at this

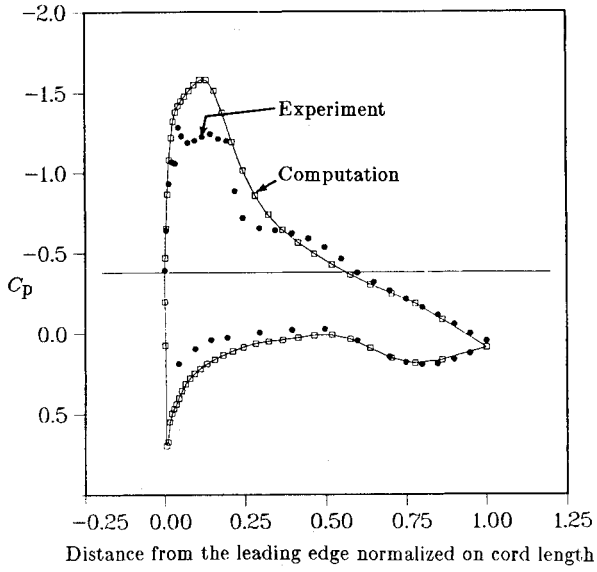

Fig. 5 C_p profiles at $y=0.6c$. Comparison with experimental data.[20]

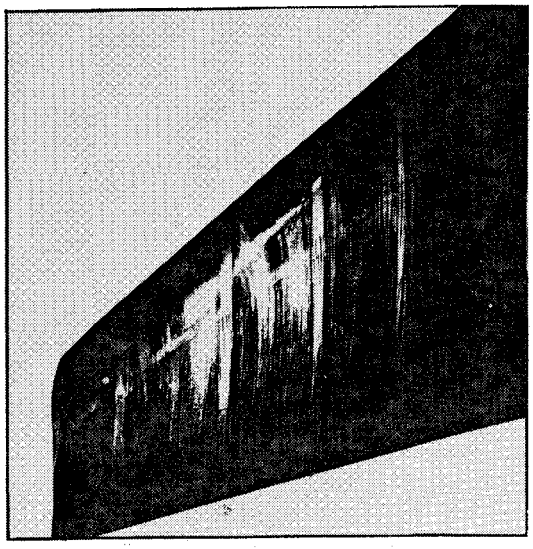

Fig. 6 Oil-flow pattern at $M=0.82$ from Ref. 20.

Mach number is the appearance of a ridge where the oil path lines change direction. The flowfield pattern from the numerical solution can be best visualized by plotting the path of particles whose motion is defined by the following equation:

$$\frac{dx}{dt}=u$$

The above equation can also be used as the definition of the streamlines. If we restrict the path of the particles to a surface, the streamlines of the projection of the velocity vector will be defined on that surface. On the surface of the wing the velocity is zero due to the no-slip condition and, hence, particles on the wing surface do not move. At one mesh ($\zeta=2$) above the surface, the velocity vector is nearly parallel to the wing surface, and by plotting the particle path in that plane the streamlines are observed close to the surface, but not the oil-flow pattern. In general, the oil film has a thickness, mass, and surface tension, and a complete simulation of the film is much more involved than massless particle tracing. Figure 7 shows the particle path pattern in the $\zeta=2$ plane (average distance to the wing $d_2=0.4\times10^{-3}c$). The appearance of a ridge is clearly seen where the paths of the particles converge. Converging lines indicate flow separation, and diverging lines indicate flow reattachment. Both separation and reattachment can be detected in Fig. 7. If the computed streamlines in that plane ($\zeta=2$) are compared with the experimental oil-film pattern, the pronounced curving of the streamlines is noted as opposed to the rather straight, streaky pattern indicated by the oil film. The difference between the two patterns may be due to the fact that the oil film has a thickness and may be protruding into the boundary layer beyond the plane at which the numerical results are presented.

Figure 8 shows the location of the separation and reattachment lines relative to the wing outline. Particles that start between the reattachment line and the wing tip are convected toward the tip vortex; particles outside that region will not be trapped by the tip vortex. The tip vortex can be clearly visualized by the three-dimensional path of the particles shown in Fig. 9. These particles are generated near the leading edge of the wing at several spanwise locations. Particles that start at a spanwise location $y<0.4c$ do not get entrapped in the tip vortex, but particles starting at $y>0.4c$ are captured in the tip vortex. The three-dimensional flow separation on the wing surface forms part of the root of the tip vortex. Figure 10 shows the tip vortex as detected by particles released close to the wing tip. The spiraling of the particles around the wing tip is clearly seen. This figure also

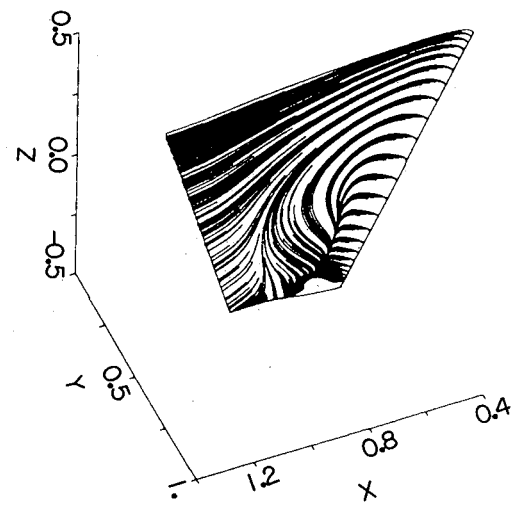

Fig. 7 Particle paths on $\zeta=2$ surface.

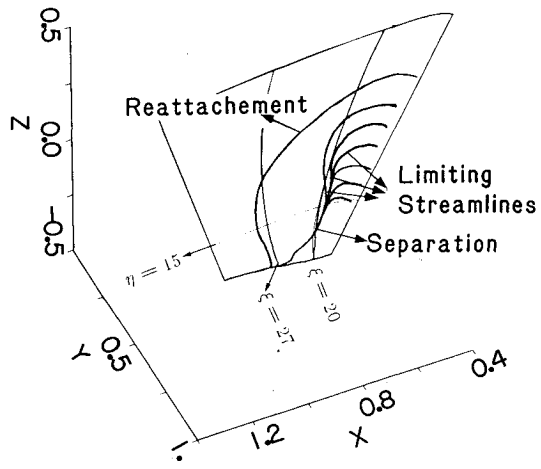

Fig. 8 Flow separation and reattachment lines.

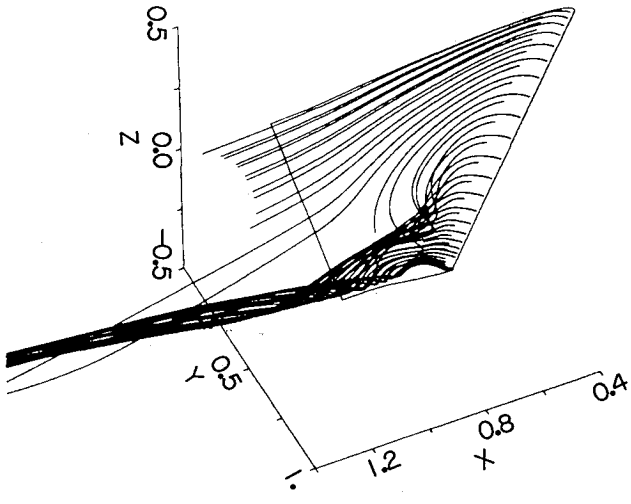

Fig. 9 Three-dimensional particle paths.

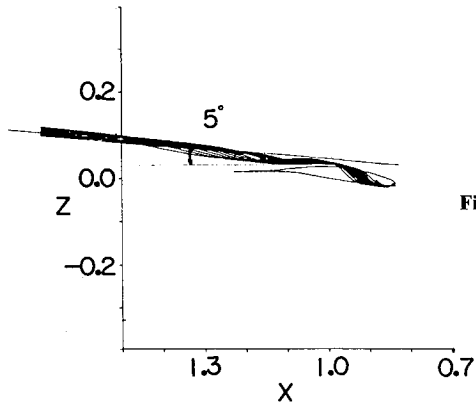

Fig. 10 Tip vortex.

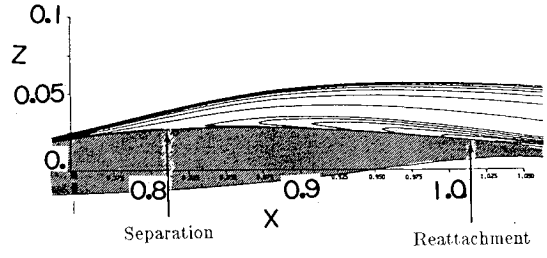

Fig. 11 Particle paths on x-z plane: surface $\eta = 15$.

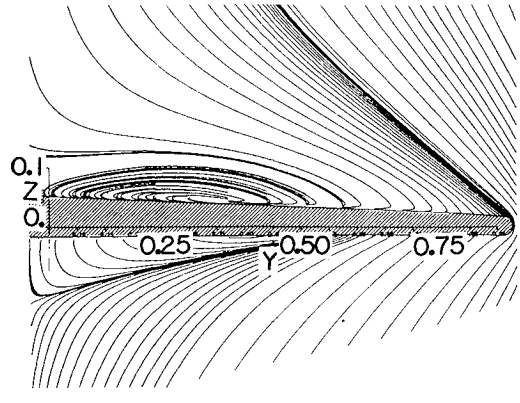

Fig. 12 Particle paths on y-z plane: surface $\xi = 20$.

shows that as the vortex lifts off the wing, the asymptotic angle reached is $\alpha = 5$ deg (the angle of attack).

The three-dimensional flowfield is usually cumbersome to analyze, and an effective way to analyze such a field is to project surface sections of the field onto appropriate two-dimensional planes. Three surfaces, $\eta = 15$, $\xi = 20$, and $\xi = 27$, were selected to study the tip vortex formation. These surfaces intersect the surface of the wing, as shown in Fig 8; that is, $\eta = 15$ is a surface cut of the flowfield that will show the flow pattern in a section more or less parallel to the streamwise direction; the other two surface cuts show the flow pattern in sections approximately normal to the streamwise direction. Figure 11 shows the particle paths describing the flowfield at $\eta = 15$ projected on the x-z plane. The flow-separation and reattachment points are indicated by the arrows. Since the flow is three dimensional, a recirculation zone is not necessary to indicate reattachment. The thickness of the separated layer is about $0.075c$ and is of the same order as the boundary layer thickness at the root of the wing; that is, the separation zone is fairly thin. Figure 12 shows the streamlines of the flowfield at $\xi = 20$ projected on the y-z plane. In this projection, the core of the recirculation zone is clearly distinguishable. If this recirculation zone is taken to be the root of the tip vortex, it can be concluded that the tip vortex is attached to the wing in this plane. The combination of the observations from vector plots and the three-dimensional particle paths (Fig. 9) indicates that the vortex line on the wing surface away from the tip is almost parallel to the leading edge. Figure 13 shows the streamlines of the flowfield at $\xi = 27$ projected on the y-z plane. At this location, the core of the vortex is much smaller, and the center of the vortex has shifted toward the wing tip and lifted from the wing surface. The direction of this vortex is downstream.

Plots of velocity vectors at different sections along the wing show that, near the wall, both the flow and the grid are nearly parallel to the wing surface, therefore, there is little crossflow with respect to the grid. This is an indication that the thin-layer approximation should still hold in this case. The smoothing terms used in the computation are fourth-order terms and, in principle, should have little effect near the walls where the viscous terms are dominant and the vortex is formed. Eriksson and Rizzi,[6] who used the Euler equations and imposed no-flux boundary conditions at the wall, as compared to the no-slip boundary conditions used in the present study, were still able to capture a tip vortex. They attribute the vortex formation to an unsteady process. These observations are an indication that the presence of the tip vortex is not turbulence-model-dependent; however, the size of the boundary layer and the separation zone are

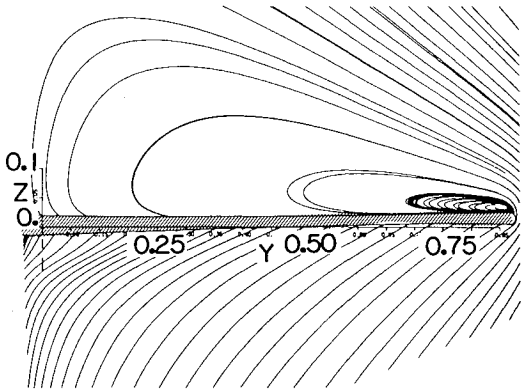

Fig. 13 Particle paths on y-z plane: surface $\xi = 27$.

dependent on the model used. To evaluate the model, more detailed experimental data are needed.

Summary and Conclusions

A computer code has been developed to solve the three-dimensional, compressible thin-layer equations in generalized coordinates. The code can accommodate up to 200,000 grid points. A modular grid-generation system has also been developed that can be used to generate one-dimensional grid stretching and two- and three-dimensional body-fitted grids. This system was used to compute the flowfield around a low-aspect-ratio wing at $M = 0.82$. At this Mach number, an oblique shock is observed on the upper surface of the wing. Also, a tip vortex forms and lifts off the wing. The formation of the tip vortex was analyzed. It was found that the flow around the leading edge contributes to the vortex formation around the tip, and the circulation generated in the boundary layer will also contribute to the formation of the tip vortex. At this Mach number, a vortex line parallel to the leading edge interacts with the tip vortex.

Acknowledgments

This work was carried out under Grant NAG 2-029 sponsored by the NASA Ames Research Center. Partial support was also provided by Prof. J. Steger, Stanford University. The author is indebted to P. Buning of NASA Ames Research Center for his three-dimensional graphics package that was used to generate the figures in this paper. Special thanks go to T. Pulliam and P. Moin, NASA Ames Research Center, for numerous helpful discussions during the course of this work.

References

[1]Prandtl, L., "Applications of Modern Hydrodynamics to Aeronautics," NASA RP-1050, edited by R. T. Jones, 1979.

[2]Subramanian, N. R., Holst, T. L., and Thomas, S. D., "Recent Applications of the Transonic Wing Analysis Computer Code TWING," NASA TM-84283, 1982.

[3]Greene, G. C., "Wake Vortex Alleviation," AIAA Paper 81-0798, 1981.

[4]Baldwin, B. S. and Lomax, H., "Thin Layer Approximation and Algebraic Model for Separated Turbulent Flows," AIAA Paper 78-257, 1978.

[5]Rizzi, A. and Eriksson, L. E., "Transfinite Mesh Generation and Damped Euler Equation Algorithm for Transonic Flow Around Wing-Body Configurations," AIAA Paper 81-0999, 1981.

[6]Eriksson, L. E. and Rizzi, A., "Computation of Vortex Flow Around Wings Using the Euler Equations," *Proceedings of the IVth GAMM Conference on Numerical Methods in Fluid Mechanics*, Vieweg-Verlag, Paris, 1981.

[7]Rizzi, A., "Mesh Influence on Vortex Shedding in Inviscid Flow Computations," *Recent Contributions to Fluid Mechanics*, edited by W. Haase, Springer-Verlag, Berlin, 1982.

[8]Mehta, U. and Lomax, H., "Reynolds Averaged Navier-Stokes Computations of Transonic Flows—The State-of-the-Art," *Transonic Aerodynamics*, edited by D. Nixon, *Progress in Astronautics and Aeronautics*, Vol. 81, AIAA, New York, pp. 297-375.

[9]Fujii, K. and Kutler, P., "Numerical Simulation of the Leading-Edge Separation Vortex for a Wing and Strake-Wing Configuration," AIAA Paper 83-1098, 1983.

[10]Hollanders, H., Lerat, A., and Peyret, R., "3-D Calculation of Transonic Viscous Flows by an Implicit Method," AIAA Paper 83-1953, 1983.

[11]Dwyer, H. A., Smooke, M. D., and Kee, R. J., "Adaptive Gridding for Finite Difference Solutions to Heat and Mass Transfer Problems," Symposium on the Numerical Generation of Curvilinear Coordinate Systems and Use in the Numerical Solution of Partial Differential Equations, Nashville, Tenn., 1982.

[12]Beam, R. M. and Warming, R. F., "An Implicit Finite-Difference Algorithm for Hyperbolic Systems in Conservation-Law Form," *Journal of Computational Physics*, Vol. 22, No. 1, 1976, pp. 87-110.

[13]Briley, W. R. and McDonald, H., "Solution of the Multidimensional Compressible Navier-Stokes Equations by a Generalized Implicit Method," *Journal of Computational Physics*, Vol. 24, No. 4, 1977, pp. 372-397.

[14]Pulliam, T. H. and Steger, J. L., "Implicit Finite-Difference Simulations of Three-Dimensional Compressible Flow," *AIAA Journal*, Vol. 18, Feb. 1980, pp. 159-167.

[15]Mastin, C. W. and Thompson, J. F., "Transformation of Three-Dimensional Body-Fitted Curvilinear Coordinate Systems for Fluid Dynamics Calculations," *Numerische Mathematik*, Vol. 29, No. 4, 1978, pp. 397-407.

[16]Thomas, P. D., "Composite Three-Dimensional Grids Generated by Elliptic Systems," *AIAA Journal*, Vol. 20, 1982, p. 1195.

[17]Thomas, P. D. and Middlecoff, J. F., "Direct Control of the Grid Distribution in Meshes Generated by Elliptic Equations," *AIAA Journal*, Vol. 18, 1980, pp. 652-656.

[18]Morel, T., private communication, Integral Technologies, Westmont, Ill., 1983.

[19]Hinson, B. L. and Burdges, K. P., "Acquisition and Application of Transonic Wing and Far-Field Test Data for Three-Dimensional Computational Method Evaluation," AFOSR-TR-80-0421, 1980.

[20]Keener, E. R., "Computational-Experimental Pressure Distributions on a Transonic, Low-Aspect-Ratio Wing," AIAA Paper 84-2092, 1984.

[21]Holst, T. L., Subramanian, N. R., and Thomas, S. D., "The Efficient Solution of Transonic Wing Flow Fields," 2nd Symposium on Numerical and Physical Aspects of Aerodynamic Flows, Long Beach, Calif., 1983.

[22]Douglas, J. and Gunn, J. E., "A General Formulation of Alternating Direction Methods," *Numerische Mathematik*, Vol. 6, 1964, p. 428.

[23]Chapman, D. R., "Computational Aerodynamics Development and Outlook," *AIAA Journal*, Vol. 17, Dec. 1979, pp. 1293-1313.